ENERGETIC CONDENSATION GROWTH OF Nb THIN-FILMS

M. Krishnan, E. Valderrama, and C. James, Alameda Applied Sciences Corporation (AASC),
San Leandro, California 94577,
X. Zhao, J. Spradlin, A-M Valente Feliciano, L. Phillips, and C. Reece, Thomas Jefferson National Accelerator Facility
(Jefferson Lab), Newport News, Virginia 23606
K. Seo, Norfolk State University (NSU), Norfolk, Virginia 23504
Z. H. Sung, Applied Superconductivity Center, Florida State University (FSU), Tallahassee, Florida 32310
F. A. Stevie, P. Maheshwari, and D. Batchelor, Analytical Instrumentation Facility,
North Carolina State University, Raleigh, NC 27695

Abstract

This paper describes Energetic Condensation Growth of Nb films using a cathodic arc plasma, whose 60-120eV ions penetrate a few monolayers into the substrate and enable sufficient surface mobility to ensure that the lowest energy state (crystalline structure with minimal defects) is accessible to the film. Hetero-epitaxial films of Nb were grown on a-plane sapphire and MgO crystals with good superconducting properties and crystal size (10mm × 20mm) limited only by substrate size. The substrates were heated to 700°C and coated at 300, 500 and 700°C. Film thickness varied from ~0.25µm to >3µm. Residual resistivity ratio (RRR) values (up to a record RRR 585 on MgO and RRR 328 on a-sapphire) vary with substrate annealing and deposition temperatures. XRD spectra and pole figures reveal that RRR increases as the crystal structure of the Nb film becomes more ordered, consistent with fewer defects and hence longer electron mean free path. A transition from Nb(110) to Nb(100) orientation on the MgO(100) lattice occurs at higher temperatures. SIMS depth profiles, EBSD and SEM images complement the XRD data. Crystalline structure in Nb on amorphous borosilicate substrates has potential implications for future, lower-cost SRF cavities.

ENERGETIC CONDENSATION

This paper describes Energetic Condensation Growth of Nb films using a cathodic arc plasma. Such a plasma uses a low voltage (~30V) arc discharge to generate a highly ionized plasma [1-3] the ions of which consist exclusively of the cathode material. The plasma is created in a vacuum arc discharge, so can be sustained in otherwise ultra-high vacuum (~10^{-8} Torr) conditions. For Nb plasmas, the ion energy spectrum has been measured [4] to lie in the range of 60-120eV, with most of the ions being triply charged. When such energetic ions impinge upon a substrate, they penetrate and deposit their energy within a few monolayers from the surface. The net energy deposited is in the range of 100-170 eV, as the ≈46 eV of ionization potential energy carried by Nb^{3+} is added to the kinetic energy. This energy range greatly exceeds typical binding energies in the lattice, so substrate atoms are displaced and the excess energy goes into electronic and phonon excitations. These ion deposition processes occur on a rapid time scale of ~1 ps. When such deposition is accompanied by substrate heating, the slower time-scale thermal diffusion allows defects to migrate to the surface where they are annihilated. Lifshitz et al [5] and Brice et al [6] have described the details of the interaction between energetic ions (~100eV) and various substrates. They have coined the term 'subplantation' to distinguish this regime of ion-surface interactions from deep implantation (>1keV ions) and surface interactions (<1eV). In subplantation, the incident ions deposit more than enough energy into just a few sub-surface atomic layers to displace atoms from the lattice and create interstitials. The key to effective subplantation is to maximize the number of displacements within this sub-surface layer, while minimizing deeper defects. This is because the ion energy deposition (that occurs on ~1-10ps time scales) must be accompanied by substrate heating. This heating allows sub-surface defects (lattice dislocations, voids and impurities) to migrate to the surface where they are annihilated. Such a synergistic interplay between the non-thermal ion deceleration physics and thermal diffusion physics promotes growth of the film in a low energy state this is likely to be epitaxial growth, evolving as the film thickens, to homo-epitaxial growth. Our pulsed discharge is fired once every few seconds, so the synergistic effects of fast ion deposition and thermal annealing are completed on each pulse.

AASC and Jefferson Lab conduct research into SRF thin-film coatings that are grown using energetic condensation (EC) a term used to represent two complementary approaches: a UHV cathodic arc process and an ECR source process. Both of these sources deliver ions to the coated surface that have ~100-200eV energy. In the case of the cathodic arc the Nb ions are triply charged and have kinetic energy spread over 60-120eV. In the case of the ECR source, the typical singly charged Nb ion energy is ~60eV. A bias of ~100-120V increases the energy to ~160-180eV at the substrate. In the case of either the vacuum arc or the ECR, the energy is easily varied by varying the substrate bias voltage.

Thornton [7] presented a Structure Zone Diagram (SZD) to describe the interplay between thermal and kinetic energy driven film growth in thin films. This SZD is applicable to processes in which the source plasma is created in a partial pressure of noble gas such as Argon. Anders [8] (see Fig. 1) has offered a variation on the SZD that is more appropriate for vacuum deposition. In this case, Thornton's pressure axis is replaced by an energy axis. Zone 2 of Fig. 1 (reproduced from Ref. 8) shows that high energy ions effectively permit low-temperature ion-

assisted epitaxial growth. This paper presents several examples of such epitaxial growth of Nb films on various substrates.

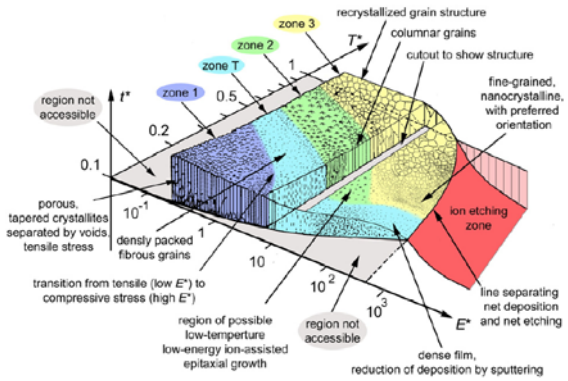

Fig. 1: SZD for ion-assisted vacuum deposition (reproduced from Ref. 8 with permission from Elsevier publishers).

MOTIVATION FOR THIN FILM DEVELOPMENT

Most RF particle accelerators worldwide utilize RF cavities made from a conventional conductor such as copper to accelerate the particle beam. A few large research accelerators such as the Continuous Electron Beam Accelerator Facility (CEBAF) at Thomas Jefferson National Accelerator Facility (Jefferson Lab, or JLab) and the Spallation Neutron Source (SNS) use superconducting radio frequency (SRF) accelerating cavities. SRF cavities consume less power than conventional cavities to produce a given accelerating gradient, even when the additional energy cost of the cryogenics system is taken into account [9]. However the cryogenics system costs do represent a significant portion of the operating expense of SRF accelerators. Operation at higher temperature would reduce those costs. Niobium, the only presently accepted superconductor for SRF accelerators, has a transition temperature T_c of 9.3K, but a practical operating temperature of 2K at the typically used 1.3–1.5 GHz RF frequencies. Operation well below T_c is required to minimize surface resistance and maximize critical magnetic field. Increasing the operating temperature of the accelerator from 2K to 4.5K could cut the cryogenics system costs in half, but would, at these rf frequencies, require use of an alternative superconductor with a higher transition temperature. Since the RF (London) penetration depth into the cavity surface is only ~50nm, it is of interest to develop thin film coatings on the nano-scale (~100nm) for particle accelerators. One approach to reducing SRF accelerator costs is to replace the expensive, bulk Nb (~$300/lb) cavities with a Nb thin film deposited on a less expensive material, such as Cu (~$3/lb) or better yet, Al (~$1/lb). The added advantage of Al over Cu is that the cavity can be cast instead of being machined, further reducing cost. Thin film coatings have the potential to reduce costs for many major upcoming SRF accelerators such as the International Linear Collider (ILC) and the Facility for Rare Isotope Beams (FRIB). Especially at the lower rf frequencies of 200-500MHz, the cavity cells are so large that bulk Nb might be prohibitively expensive, so Nb coated Cu or Cu alloys might be the more cost-effective option for operation at 4.5K [10].

Pioneering work [11,12] on Cu cavities coated with Nb thin film has been done at the European Organization for Nuclear Research, known as CERN. By 1998, 272 copper 352 MHz cavities, Nb thin film coated via magnetron sputtering, were deployed for the Large Electron-Positron Collider (LEP-II) project. The circular LEP-II collider, with a circumference of 27 kilometers, was one of the largest particle accelerators ever constructed and has recently been replaced by the Large Hadron Collider (LHC). Future accelerator facilities, such as the proposed International Linear Collider (ILC), require high accelerating field ~35 MV/m and $Q \geq 10^{10}$. It was reported [13,14] that at 1.7K the Nb thin film cavities for LEP had Q-drop to below 10^{10} at ≈15MV/m and to below 5×10^9 at ≈20 MV/m. There is a motivation to better understand these limits and to improve Nb thin films' performance for future SRF accelerator cavities.

The payoff of higher temperature SRF cavities and cavities made out of thin-film coated Cu or Al has motivated a multi-year research program at Alameda Applied Sciences Corporation (AASC). The goal is to utilize energetic condensation to produce Nb-on-Cu films of sufficient quality to determine if the thin film RF properties are adequate for high power SRF applications such as particle accelerators. Thorough characterization of the surface morphology and RF properties of Nb-on-Cu is a necessary first step toward qualifying Nb coated Cu SRF cavities. Given the high-cost (>$100M) and infrequent occurrence of large SRF accelerator upgrades and construction, it is difficult to imagine acceptance of an alternative superconductor in SRF accelerators without demonstrated performance equivalent to (or better than) that of bulk Nb (2K). Implementation of Nb-on-Cu coated cavities into commercial accelerators, our long-term goal, is likely to follow reliable operation in a research laboratory setting.

EXPERIMENTAL CONFIGURATION

There are two experimental configurations at AASC. Fig. 2 shows a photograph of the Coaxial Energetic Deposition (CED™) apparatus with a 2.2 GHz copper RF cavity adjacent to it, shown for scale.

Figure 3 is a schematic drawing of the operation of the CED™ apparatus. The arc is formed between an on-axis cathode (1-cm diameter and 60-cm long) and a coaxial mesh anode (4-cm diameter and 45-cm in length). The arc is sustained by a PowerTen, Inc. power supply (100V, 200A). The repetition rate of the arc is 0.25Hz, limited at present by SCR switches in the trigger circuit, but may be increased by using IGBT switches. The arc is triggered by a proprietary trigger system.

Fig. 2: Photograph of the CED™ system, showing a 2.2 GHz copper RF cavity for scale.

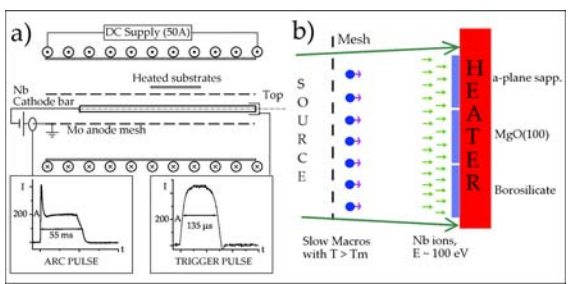

Fig. 3: Schematic drawing of CED™ operation: (a) coaxial electrode geometry and typical current pulses to trigger and arc; (b) detail of anode mesh and heated substrate, showing plasma transmitted by the anode onto the substrate.

The substrate is placed outside the mesh anode. The entire assembly is enclosed in a 25-cm dia. CF vacuum spool. The vacuum spool is double-walled with a solenoid wound on the outside. The solenoid is capable of producing a peak magnetic field of 10mT in either the z^+ or z^- direction. The arc current is controlled by adjusting a ballast resistor in series with the cathode. This system is equipped with a substrate heater and temperature control system that is capable of operation up to 1200 ºC. The key process variables are substrate temperature, degree of annealing, substrate bias, deposition rate, and base pressure. Base pressures of ~$5x10^{-9}$ Torr are possible within this chamber and are measured and monitored using a SRS200 residual gas analyzer (RGA). In addition to substrate temperature control, the substrate can also be biased.

Figure 4 shows a photograph of the Cathodic Arc Deposition (CAD) facility available at AASC.

Fig. 4: Photograph of Cathodic Arc Deposition (CAD) facility at AASC.

Two Pulse Forming Networks (PFNs) are shown in the figure. These PFNs allow independently triggered arcs to be driven in two separate cathodes, with a common mesh anode. Figure 5 shows a photograph of the dual-target arrangement. This arrangement allows growth of superconducting films of A-15 compounds such as Nb_3Sn, Mo_3Re[15] etc., as well as MgB_2 films.

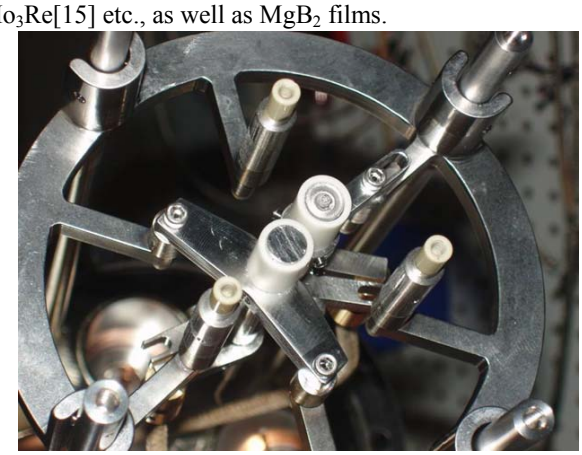

Fig. 5: Photograph of dual-cathode Cathodic Arc Deposition (CAD) facility at AASC.

The film deposition rate in the CAD source was measured by measuring the thickness profile of a deposited Nb film. A 75-mm diameter masked borosilicate glass witness plate was located 40-mm from the 10-mm diameter cathode. After 7000 pulses of 500A/1ms, the thickness profile shown in Fig. 6a was obtained using a DEKTAK profilometer.

Simple book-keeping allows determination of the growth rate as shown in Fig. 6b. The Nb plasma is formed from tiny cathode spots that typically carry ~100A at most. Each spot lasts for ~1µs and hence the spots dance all over the 10-mm diameter cathode during the 1ms pulse. Viewed from afar, the plasma appears to emanate from a ~10-mm spot. The expansion into vacuum of such a plasma is supersonic and the plasma expands into a cone of half-angle ≈30°. The red curve in Fig. 6a is a Gaussian Fit to the thickness profile. The integral of the mass under

this profile was calculated as 7.3µg/pulse, as shown in the first row of the Table in the figure.

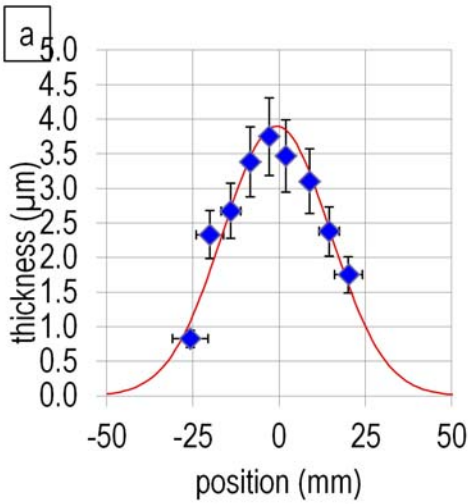

vol under gaussian=	0.006	cc
mass under gaussian=	0.051	g
b mass/shot=	7.3	µg
charge/shot=	0.5	C
anode transission.=	0.7	
erosion rate=	21	µg/C
peak thickness/pulse=	0.56	nm
instant. rate=	560	nm/s
instant. flux of Nb ions=	1.0E+18	Nb ions/cm^2-s

Fig. 6: Measured Nb film thickness profile (a) and derived growth rate (b) for CAD coating apparatus.

From the known charge/pulse and the transparency of the mesh anode, the erosion rate of Nb at the cathode was estimated to be 21µg/C, a value that agrees with published literature[16]. The next row of the table shows the peak film thickness/pulse, as 0.56nm. Note that this is ≈1 atomic layer/pulse. But the pulse lasts only 1ms. Hence the instantaneous deposition rate is 560nm/s. To put this in perspective, the instantaneous flux of Nb ions (triply charged) to the substrate may be estimated from the mass deposited/pulse, the effective spot size over which this mass is deposited and the pulse width. The estimated flux is 10^{18} Nb ions/cm^2-s. Such a high flux, combined with the high energy deposited into the first few monolayers of the substrate, is capable of significant modification of that surface. Nb ions will be deposited into the substrate as interstitials, displacing existing atoms and forcing a re-arrangement of the lattice. Under the right conditions of substrate annealing and heat treatment, epitaxial growth of the Nb film is observed. But what happens to this hetero-epitaxy when the Nb grows on a dissimilar substrate such as sapphire, MgO or Cu? At the rate of 0.56nm/pulse, after just ten pulses, a layer of ≈5.6nm will have grown. Subsequent pulses deliver Nb ions that deposit their energy into a sub-surface layer that consists almost exclusively of Nb atoms. Our films are typically ~1-5µm thick. Thus although the initial stage of growth of the Nb film is denoted as hetero-epitaxy, for thicker films, the growth transitions from hetero- to homo-epitaxy after a certain film thickness. Energetic condensation drives this transition and enables pure crystals of Nb to be grown on rather dissimilar substrates, as shown below. The deposition rate is easily controlled since the mass liberated from the cathode is directly related to the total charge transferred by the arc. The charge transfer increases by increasing the magnitude and/or the duration of the current.

SOME ASPECTS OF CRYSTAL GROWTH USING ENERGETIC CONDENSATION

Nb thin-film depositions were carried out in the CED™ apparatus on a-plane and c-plane sapphire, MgO, borosilicate glass and Cu substrates. The sapphire, MgO and borosilicate coatings allowed measurements of RRR to be made, whilst the Cu coatings were used to study the influence of substrate temperature on film quality. Several tools were used to characterize the films: SEM, XRD, EBSD, cross-section EBSD, TEM, AFM and SIMS. RRR data are to be published elsewhere [17]. One example of a high RRR 585±1%, measured in a 5.5µm thick film of Nb on MgO (100) is shown in Fig. 7.

RRR 330 was measured on a-sapphire and RRR 43 on c-sapphire. We also measured RRR 31 in a Nb film grown on an inexpensive borosilicate glass sample (purchased from McMaster and used as witness surfaces for our thickness measurements), when it was heated to 500°C. These Nb films were ~2-3µm thick. A multiple-sample, four-point-probe testing platform was used to measure thin film materials' residual resistivity ratio (RRR). The RRR is defined [18] as the ratio of resistivity at 300K to that at 10K. An ac or dc current runs through the sample via two poke pins (#1 and #4), and the small voltage signal dropped on two intermediate poke pins (#2 and #3) is measured using either a high-speed high-dynamic-range data acquisition system (National Instruments™), or a commercial lock-in amplifier (Stanford Instruments™ SR530), or a commercial nano-voltmeter (Keithley™). The processes of sample-multiplexing, data acquisition, and temperature recording are controlled using a customized LabVIEW™ automation program. Since the pin 2-3 differential voltage is proportional to the material's resistivity, RRR is measured as the ratio of the differential voltage at 300 to that at 10K. The test fixture and up to 16 samples were inserted into a vacuum sealed Dewar and cooled by liquid helium down toward 4K. By warming up the samples slowly, the pin 2-3 differential voltage was recorded as a function of temperature, which was measured by a Lakeshore Cernox™ sensor (resolution ~10mK). The overall RRR measurement error is 2-10%.

Since we found that RRR increases strongly with film thickness [17], it is likely that by making the Nb film on borosilicate thicker, we might push towards the RRR 100

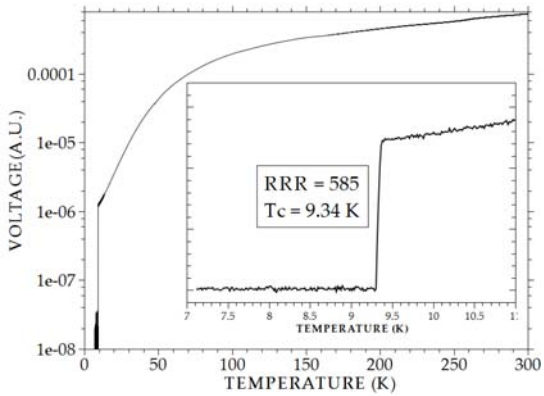

Fig. 7. RRR 585 in 5.5μm Nb film grown on (100) MgO.

level where the film might become practical for SRF applications. Later we show that not only did the RRR increase in Nb-on-borosilicate as the temperature was increased, but that the degree of crystallinity of the film also increased. This result, obtained on an amorphous substrate, is of particular significance to future SRF cavities formed from low-cost cast Al, that would also offer an amorphous surface for film growth. In the rest of this paper, we focus attention on several interesting aspects of crystal growth by energetic condensation.

XRD data from Nb films on a- and c-sapphire

Figure 8 shows XRD Pole Figures measured from Nb films that were grown on a-sapphire substrates. A typical deposition was preceded by annealing the substrate at 700°C for three hours, then growing the Nb film using the CED apparatus at various deposition temperatures. The principles of pole figure surveys can be found in an X-Ray Diffraction textbook [19]. For pole figure measurements, a point focus crossed-slit collimation was used. The secondary optics consisted of a 0.27° parallel-plate collimator followed by a flat graphite secondary monochromator and a proportional detector. A Soller slit was placed in front of the detector. Besides the conventional Bragg-Brentano survey (also known as the θ /2θ survey), XRD pole figures in stereographic projection format were used to investigate "texture" (grain distribution in-plane) of every sample. A crystal plane in the 'real lattice space' is a point in the 'reciprocal lattice space'. The XRD pole figure technique uses a scattering vector to map such "points" in reciprocal lattice space. The difference between a diffracted and incident X-ray wave-vector is defined as scattering vector. In pole figure coordinates, φ (0-360^0) is the azimuth angle in-plane; ψ (0-90^0) is the tilting angle between the scattering vector and the normal to the substrate surface. In such measurements, a scattering vector is programmed to gyrate in both coordinates to survey the positive hemispherical volume of a reciprocal lattice space. A film with random orientation would give a uniform distribution of scattering intensity. A single crystal film displays a spot pattern, and a film with restricted fiber texture displays a ring pattern of modulated intensity, tending

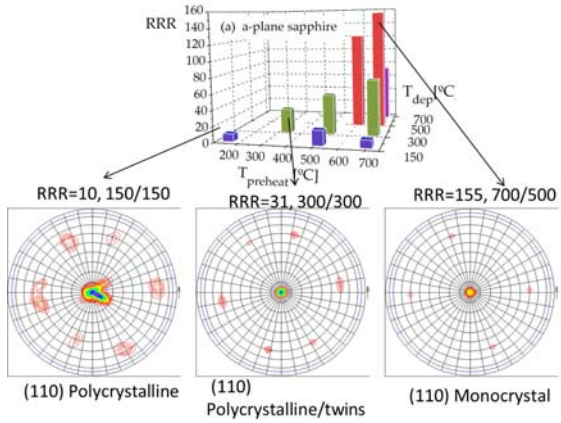

Fig. 8: XRD Pole Figures for Nb films grown on a-sapphire.

toward a spot pattern with increasing degree of orientation.

Note that the diffuse peaks in the (110) pole figure for RRR 10 become much sharper (less texture) at RRR 31. The six lobes visible around the central pole in the figure are associated with twin symmetry in the epitaxial crystal, and are discussed elsewhere [20]. At the highest RRR 155, the sharpness of the lobes in the pole figure indicate that the Nb thin film is a single crystal with (110) crystal plane parallel to the substrate surface. The high crystallinity at the highest RRR might suggest fewer impurities and defects in the Nb lattice. These results demonstrate the ability to tailor the crystal structure and RRR (hence defect and impurity concentrations) of Nb films by control of substrate thermal conditions, along with use of energetic condensation. Nb-on-MgO substrates showed a similar picture of better crystallinity with higher RRR and a remarkable transition from (110) to (100) orientation. Those results are published elsewhere [17].

Figure 9 shows Pole Figures for a Nb film grown on c-sapphire.

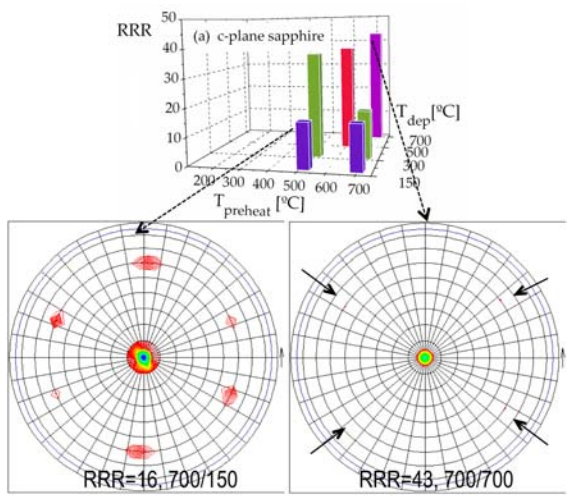

Fig. 9: XRD Pole Figures for Nb films grown on c-sapphire.

As the RRR increases with substrate temperature from RRR 16 at 700/150 to RRR 43 at 700/700, the pole figures show a sharp transition from a rather diffuse (polycrystalline) structure to a sharp, single crystal Nb layer. The poles are so sharp at RRR 43 that arrows are used to guide the reader to their locations.

The XRD pole figures represent crystal structure averaged across the film thickness, as the Cu K-α x-rays used penetrate the film and even the underlying substrate. By contrast, EBSD images show only surface grain and crystal structure and are discussed next.

EBSD images from Nb films on MgO

Figure 10 shows EBSD images superimposed upon SEM images of a Nb film grown on MgO, RRR 196 (500/500). The XRD pole figure is inset at bottom right.

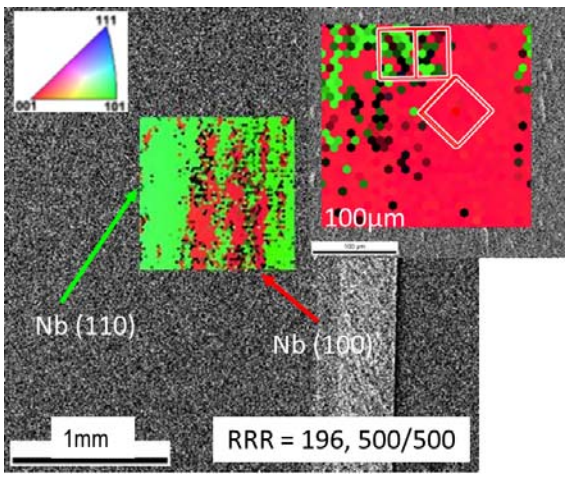

Fig. 10: EBSD images (superimposed upon SEM images) of Nb film on MgO(100) substrate.

The triangle at top left shows the color code. The crystal structure consists of a mix of (110) and (100) orientations, shown at the 1mm and 0.1mm scales. The pole figure also shows this and suggests that the crystal structure is determined early in the film growth, but a cross-section EBSD image is needed to corroborate this assertion. Such cross-section EBSD images are shown in the next section.

But first we show EBSD images taken from a higher RRR 333 sample, in Fig. 11. The inset at bottom right shows a pole figure for a similar film but one that was coated at 700/700 and gave a RRR 316. At this higher RRR the Nb film has become a single crystal across the entire 10x10mm substrate surface. The size of this crystal is limited only by the substrate size in this case. The EBSD (surface) image shows a pure (100) orientation. The pole figure in this case captures only the (200) plane, but that is in the same family as the (100) plane.

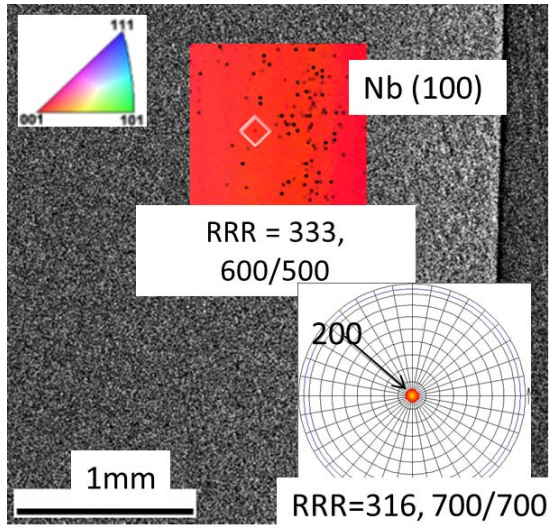

Fig. 11: EBSD image (superimposed upon SEM images) of Nb film (600/500) on MgO(100) substrate. XRD pole figure (700/700) is at bottom right.

Cross-section EBSD images of thin-films

Figure 12 shows a cross-section EBSD image of a portion of a Nb film grown on MgO at 150/150 with RRR 7.

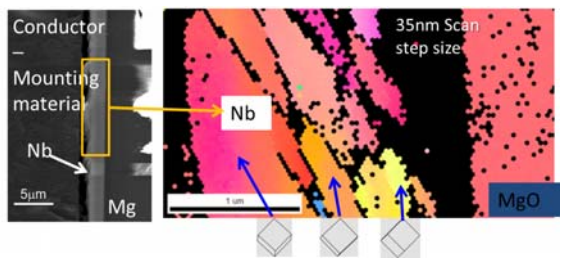

Fig. 12: Cross-section EBSD image of Nb film (150/150) on MgO, RRR 7.

Starting from the MgO (001) substrate at the right, one observes a 0.2µm black layer. This layer is black because the EBSD software makes it black if the Confidence Index (CI) is <0.2. This could indicate grain size too small to be resolved by the instrument (<50nm). After this black layer, a mix of (001) and (101) planes are observed to grow at an angle to the substrate (yellow and pink in the inset in the figure), and appear to grow larger as the film thickens. The low substrate temperature in this case does not allow large grain crystal growth right from the surface. However, even for this low temperature case, despite poor annealing of defects by heating, we see the effects of energetic condensation for thicker films. Beyond about 0.2µm, the film gradually acquires epitaxial crystal growth. Since the black layer below the crystal is almost purely Nb, it is more appropriate to describe such growth as homo-epitaxy. However, because the 'seed' for nucleation and grain growth is a poor seed in this case, the subsequent crystal growth probably has a high defect density, poor inter-grain boundaries and results in a low RRR 7. Figure 13 shows a dramatic difference at 500/500, when the RRR increased to 196.

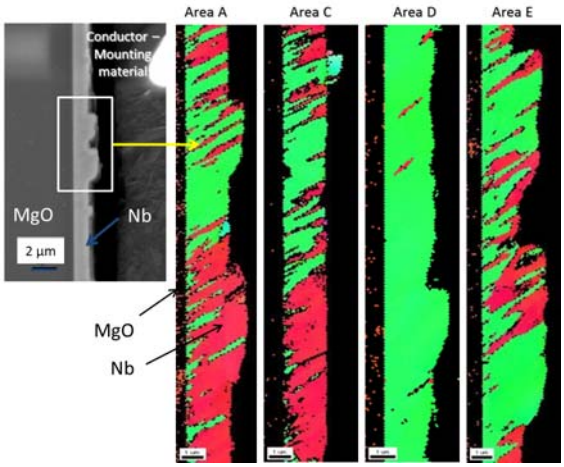

Fig. 13: Cross-section EBSD image of Nb film (500/500) on MgO, RRR 196.

To keep the reader on her/his toes, we have reversed the SEM reference image in this case, so that the MgO is at left and the Nb film is to the right. In stark contrast to the image of Fig. 12, the Nb crystal growth begins immediately at the MgO surface. Cross-section EBSD images from four different locations on the film are presented, although only Area A shows its associated SEM image. In each case, the Nb epitaxy is observed to be a mix of (001) and (101) (equivalent to 100 and 110 planes) beginning at the substrate surface. Area E shows that the grains grow larger with thickness. Area D shows an almost uniform 110 orientation. These cross-section images view the crystal orthogonal to the direction of view of the surface EBSD, so the crystal planes plotted in the two cases will not correspond. But they do corroborate the surface images presented in Fig. 10 and suggest that RRR increases with thickness because the grains become larger and defects are reduced.

Figure 14 shows the cross-section images from Nb-on-MgO at 700/700, RRR 316. Here the cross-section images indicate a uniform crystal orientation across the field of view. The smaller image to the right shows a finer scan using 150nm steps, taken over a limited field of view indicated in the white square in the EBSD image to its left. The black zone indicates a poor CI that might be simply due to the grains being too small to be resolved. The 150nm step-size scan shows that the highly crystalline Nb film grows around this impurity region and envelopes it. Beyond its surface, a pure crystal growth is observed. Again, we observe the synergistic effects of thermal annealing and energetic ion deposition in the film growth. What is not revealed at this resolution is microscopic defects in the growing lattice that are gradually washed out as the film becomes thicker. That would potentially account for the strong dependence of RRR on film thickness

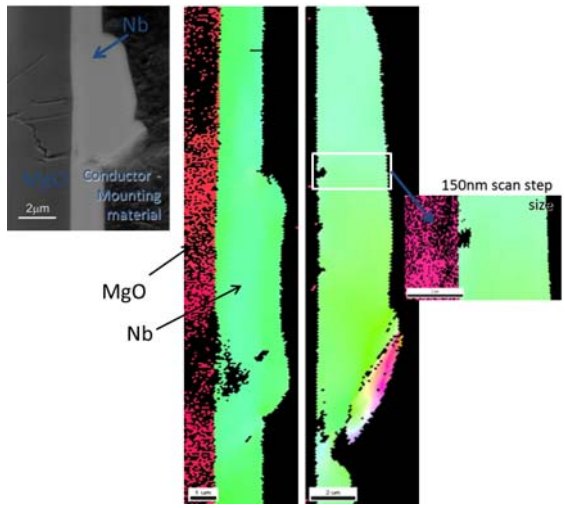

Fig. 14: Cross-section EBSD images of Nb film (700/700) on MgO(100) substrate.

Comparison of Nb thin films with bulk Nb cavities

Kneisel et al [21,22] present Q-slope and quench data for several RF cavities fabricated out of small-grain, larger-grain and single crystal Nb sheet metal. These authors describe a major difference in performance between single crystal/large grain cavities with primarily the (110) orientation at the surface vs. (100). The (110) crystal cavity showed greater surface roughness after BCP treatment and a Q-drop that did not disappear after even 12 hours of heat treatment. By contrast, the cavity with the (100) orientation had a smoother surface after BCP and gave the lowest Q-drop and highest quench fields of all cavities tested. Baars et al [23] describe the different response to BCP chemicals of different Nb crystal orientations. Our results suggest the possibility of coating existing bulk Nb cavities with a thin film of Nb that is preferentially of the 100 orientation, thereby enhancing its high field performance.

TEM and AFM images

Figure 15 shows a TEM image of a RRR 316 Nb film on MgO.

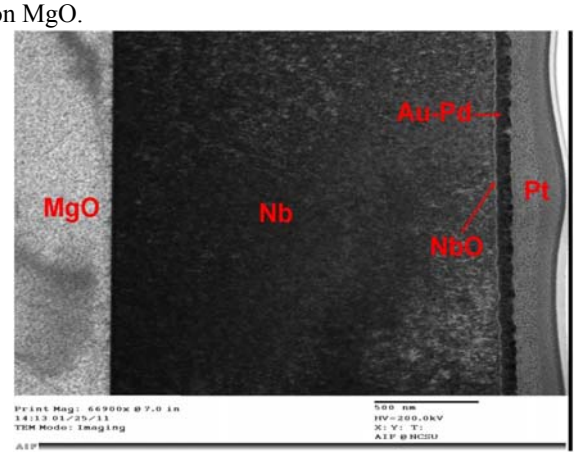

Fig. 15: TEM image of RRR 316 Nb film on MgO.

The figure shows a very smooth interface between the MgO and Nb (note the 500nm scale bar). The film appears dense and well adhered to the surface.

Figure 16 shows AFM images of three Nb films (RRR 7, 196 and 316) all grown on MgO. The surface roughness appears to be increasing with RRR.

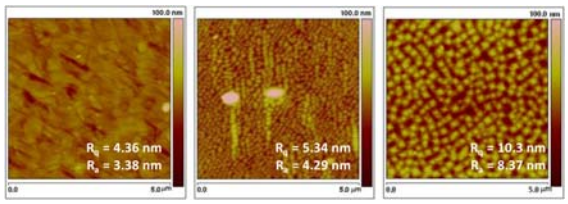

Fig. 16: AFM images of RRR 7, 196 and 316 Nb films on MgO.

Macro-particle epitaxy in Nb films

Figures 13 and 14 show what appear to be lumps on the Nb surface. These are macro-particles that are emitted by the vacuum arc, move more slowly than the ions and impinge upon the substrate. Figure 17 shows a Laser Confocal Scanning Microscope image taken of a portion of the surface of the RRR 316 Nb film grown on MgO.

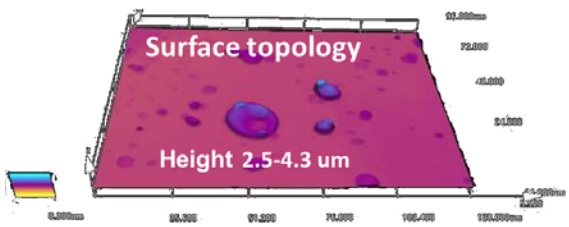

Fig. 17: Laser Confocal Scanning microscope (Olympus LEXT) image of RRR 316 film.

The two macro-particles imaged vary in height from 2.1-4.5µm and are about 10µm in diameter. These macro-particles are molten droplets of Nb emitted at the arc cathode surface that fly from the cathode to the substrate and land there. Since these particles do not penetrate the surface as do the ~100eV ions, it is interesting to ask what the crystal growth modes might be in such particles, as opposed to that of the fast ions.

Figure 18 shows two cross-section SEM images taken after FIB milling of the RRR 7 and RRR 316 films. For the lower RRR 7 film, the cross-section SEM shows fibrous, columnar texture in the 2.6µm thick film. What is remarkable is that this fibrous texture continues into the 3µm thick macro-particle that has landed on the film's surface. With reference to Anders' SZD (see Fig.1) the macro-particle occupies a region near the top left of the SZD, with the homologous temperature ratio, T/T_m~1 and very low kinetic energy. In fact, since the local pressure at the cathode spots in vacuum arcs is very high (~1000 Bar), the melting point will be increased and hence the molten macros might leave the cathode at T/T_m>1. Simple estimates show that radiation from the macro-particle surface is negligible compared to the stored enthalpy, so the macro arrives at the substrate at its emitted temperature. According to the SZD, such a particle will re-crystallize at the surface and acquire grain structure from the underlying substrate. Since the underlying substrate has fibrous, columnar grains (at RRR 7) so does the condensing macro-particle. The columnar grains increase in size with height in the film, which is consistent with increase of RRR with thickness.

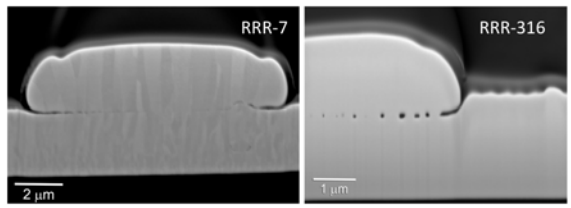

Fig. 18: FIB/Cross-section SEM images of Nb films on MgO.

However, at RRR 316, the macro-particle appears to acquire the single crystal, large grain, homo-epitaxial structure of the (100) Nb film that is beneath it. This observation suggests that once the 'seed' layer of Nb has been grown using energetic condensation, subsequent growth maintains the properties of the seed, when slow moving, massive particles land on such a seed layer. In principle, one might first create the high quality, single crystal seed of Nb on a cavity surface, then spray high purity molten Nb on to this surface, to grow very large, single crystal Nb films.

SIMS DEPTH PROFILES

SIMS analyses were obtained using a CAMECA IMS-6F with Cs^+ beam which provided best sensitivity for H, C, O, N and electronegative elements. Two samples were analyzed: (1) a RRR 333 Nb film grown on MgO; (2) a bulk sample similar to that used in SRF cavities, with RRR>300. The SIMS depth profiles show 3-4 orders of magnitude lower H content in the thin film than in the bulk Nb sample [24,25]. Several mechanisms acting simultaneously [25] might account for this significant difference between bulk and thin film Nb, such as: grain boundary distribution and motion as the film becomes thicker, that minimize impurity diffusion; the film becomes denser with time; fresh, highly reactive Nb on the walls of the chamber acts like a getter to reduce the background pressure, the high instantaneous deposition rate inhibits impurity inclusion in the film. The significantly lower H content in our films suggest that they are denser and point to a possible post-bake coating of bulk Nb cavities with our CED thin films, to make them less prone to H poisoning and other deleterious impurities. The SIMS sputtering rate was observed to be slower for the (100) film, suggesting a denser film, which is consistent with lower impurities and higher RRR.

DISCUSSION

This paper has presented examples of Nb thin films grown on various crystal substrates using energetic condensation. The term energetic condensation applies to subplantation, i.e. deposition of incident ion energy within the first few sub-surface atomic layers in a surface. The

deposition used a cathodic arc discharge that produces a plasma of pure Nb with a kinetic energy spread of 60-120eV, plus 46eV of ionization potential energy, resulting in ≈100-170eV energy deposition into the substrate. Each pulse deposits roughly one atomic layer of Nb in 1ms on the substrate. This high instantaneous deposition rate minimizes impurity contamination of the film. The energetic condensation creates dense films that adhere well to the substrate. When energetic condensation is accompanied by substrate heating, the synergistic effects of the fast ion deposition and the slower thermal annealing results in a very low-defect, epitaxial film growth. The RRR was measured on a- and c-sapphire substrates as well as on MgO. Record values of RRR 338 on a-sapphire and RRR 585 on MgO are reported. RRR is found to depend strongly upon substrate temperature. The RRR is found to also depend upon film thickness. A simple model [17] shows that the RRR at the surface of the thick films might be still higher, RRR 680 for 3μm Nb films on MgO. XRD Pole Figures reveal that the crystal structure also depends strongly on substrate temperature, becoming more ordered and single-crystal as temperature is increased. On MgO, a transition from a mix of 110 and 100 planes at 500°C to purely 100 orientation at 700°C is correlated with higher RRR. The 100 crystal is denser and harder than the 110 crystal, as evidenced by SIMS depth profiling. Both surface EBSD and cross-section EBSD (OIM) images corroborate the picture suggested by the bulk XRD data, of better crystal structure leading to higher RRR at higher temperatures and for thicker films. Cross-section SEM images of the films (sliced using a FIB apparatus) revealed that when molten macro-particles of Nb land on the film grown using ion-assisted energetic condensation, the crystal structure in the condensing macro-particle is identical to that of the Nb substrate below it. This suggests another approach to cavity coating in which a high quality 'seed' layer of Nb is first grown using our energetic condensation apparatus that is followed by simpler condensation of molten Nb metal spray on the seed layer, thereby growing very large cladding layers inside cavities. This would be an alternative to the pioneering work done at DESY on Nb clad Cu and Cu0.15%Zr cavities [26,27].

ACKNOWLEDGMENTS

This research is supported at AASC by DOE via Grant DE-FG02-08ER85162 and Grant DE-SC0004994. The JLab effort was provided by Jefferson Science Associates, LLC under U.S. DOE Contract No. DE-AC05-06OR23177 including supplemental funding provided by the American Recovery and Reinvestment Act.

REFERENCES

[1] I. G. Brown, "Vacuum arc ion sources", Rev. Sci. Instrum. 65 (10): 3061, 1994.

[2] A. Anders, Plasma and ion sources in large area coating: A review, Surface & Coatings Technology 200, (2005), 1893-1906.

[3] M. Krishnan, M. Geva and J. L. Hirshfield, "Plasma Centrifuge," Phys. Rev. Lett. 46, 36(1981).

[4] A. Bendavid, P. J. Martin, R. P. Netterfield, G. J. Sloggett, T. J. Kinder, and C. Andrikidis, "The deposition of niobium, NbN and Nb2O5 films by filtered arc evaporation," Journal of Materials Science Letters, vol. 12, no. 5, pp. 322-323, 1993.

[5] Y. I.ifshitz, S. R. Kasi, and J. Rabalais, Subplantation model for film growth from hyperthermal species, Physical Review B Vol. 41, Number 15, 15 May 1990-II.

[6] D.K. Brice, J.Y. Tsao and S.T. Picraux, Nuclear Instruments and Methods in Physics Research B44 (1989) 68-78, North-Holland.

[7] C. Thompson, "Stress and grain growth in thin films," Journal of the Mechanics and Physics of Solids, vol. 44, no. 5, pp. 657-673, 1996.

[8] A. Anders, Thin Solid Films 518 (2010) 4087–4090.

[9] E. Hand, Nature, Vol 456|4 December 2008.

[10] H. Padamsee, SRF FOR NEUTRINO FACTORIES, The 10th Workshop on RF Superconductivity, 2001, Tsukuba, Japan.

[11] C. Benvenuti, P. Bernard, D. Bloess, G. Cavallari, E. Chiaveri, N. Haebel. J. Hilleret, J. Tuckmantel, W. Weingarten, In Superconducting niobium sputter-coated copper cavity modules for the LEP energy upgrade, New York, NY, USA, 1991; IEEE: New York, NY, USA, 1991; pp 1023-5.

[12] C. Benvenuti, N. Circelli, M. Hauer, Niobium films for superconducting accelerating cavities. Applied Physics Letters 1984, 45, (5), 583-4.

[13] S. Calatroni, 20 Years of experience with the Nb/Cu technology for superconducting cavities and perspectives for future developments. Physica C 2006, 441, (1-2), 95-101.

[14] R. Russo, Quality measurement of niobium thin films for Nb/Cu Superconducting RF cavities. Meas. Sci. Techno. 2007, 18, 2299-2313.

[15] E. Valderrama, C. James, M. Krishnan, X. Zhao, K. Seo, F. A. Stevie and P. Maheshwari, "Mo-Re films for SRF applications", Proceedings of 15th International Conference on RF Superconductivity, Chicago, USA(2011), THPO077.

[16] A. Anders, "Ion charge state distributions of vacuum arc plasmas: The origin of species," Physical Review E, vol. 55, no. 1, pp. 969-981, 1997.

[17] M. Krishnan, E. Valderrama, B. Bures, K. Wilson-Elliott, X. Zhao, L. Phillips, Anne-Marie Valente-

Feliciano, Joshua Spradlin, C. Reece and K. Seo "Very high residual-resistivity ratios of heteroepitaxial superconducting niobium films on MgO substrates," Superconductor Science and Technology (to be published).

[18] H. Padamsee, J. Knobloch, and T. Hays, RF Superconductivity for Accelerators, John Wiley & Sons, Inc. 1998.

[19] B. D. Cullity and S. R. Stock, "Elements of X-ray diffraction" Chapter 14, (Prentice Hall, NJ 2001).

[20] X. Zhao, L. Philips, C. E. Reece, K. Seo, M. Krishnan and E. Valderrama "Twin Symmetry Texture of Energetically Condensed Niobium Thin Films on Sapphire Substrate (a-plane Al_2O_3)," Journal of Applied Physics.

[21] P. Kneisel, "Progress on Large Grain and Single Grain Niobium", SRF07, Beijing, Oct. 2007, TH102; http://accelconf.web.cern.ch/AccelConf/srf2007/PAPERS/TH102.pdf.

[22] P. Kneisel, G. Ciovati, W. Singer, X. Singer, D. Reschke, A. Brinkmann, PERFORMANCE OF SINGLE CRYSTAL NIOBIUM CAVITIES, Proceedings of EPAC08, Genoa, Italy, MOPP136.

[23] D. Baars et al., "Crystal orientation effects during fabrication of single or multi-crystal Nb SRF cavities", SRF07, Beijing, Oct. 2007, TH102, http://accelconf.web.cern.ch/AccelConf/srf2007/PAPERS/TUP05.pdf.

[24] Surface Analysis of Nb Materials for SRF Cavities, P. Maheshwari, H. Tian, C. Reece, G. Myneni, F. Stevie. M. Rigsbee, A. Batchelor, D. Griffis, Surf. Int. Analysis 43, 151-153 (2011).

[25] E. Valderrama, C. James, M. Krishnan, X. Zhao, L. Phillips, C. Reece and K. Seo, "High RRR Thin Films of Nb Produced using Energetic Condensation from a Coaxial, Rotating Vacuum Arc Plasma (CED^{TM})", Cryogenic Engineering Conference & International Cryogenic Materials Conference, Washington, CEC-ICMC-11, USA, June 2011.(in press).

[26] W. Singer. Seamless Cavities. 13th International Workshop on RF Superconductivity, October 15-19, 2007, Beijing, China.

[27] X. Singer, W. Singer, I. Jelezov, A. Matheisen, DESY, P. Kneisel, "HYDROFORMING OF MULTI-CELL NIOBIUM AND NbCu-CLAD CAVITIES", Proceedings of PAC09, Vancouver, BC, Canada, http://trshare.triumf.ca/Epac09proc/Proceedings/papers/tu5pfp055.pdf.